

1 **Tropopause Evolution in a Rapidly Intensifying Tropical Cyclone: A Static**
2 **Stability Budget Analysis**

3 Patrick Duran* and John Molinari

4 *University at Albany, State University of New York, Albany, NY*

5 *Corresponding author address: Department of Atmospheric and Environmental Sciences, Univer-
6 sity at Albany, State University of New York, 1400 Washington Avenue, Albany, NY.

7 E-mail: pduran2008@gmail.com

ABSTRACT

⁸ We have some cool results!

9 **1. Introduction**

10 Perhaps introduce upper-tropospheric static stability and its relationship to the diurnal cycle
11 before going into Patricia? Include references to Dunion, Navarro, and O'Neill here.

12 After undergoing a remarkably rapid intensification (RI), Hurricane Patricia (2015) set a new
13 record as the strongest tropical cyclone (TC) ever observed in the Western Hemisphere (Kimber-
14 lain et al. 2016; Rogers et al. 2017). High-altitude dropsonde observations taken by the Tropical
15 Cyclone Intensity (TCI) Experiment captured this RI in unprecedented detail (Doyle et al. 2017).
16 These observations revealed remarkable changes in the structure of the cold-point tropopause and
17 upper-level static stability as the storm intensified (Duran and Molinari 2018). At tropical storm
18 intensity, shortly before RI commenced, a strong inversion layer existed just above Patricia's cold-
19 point tropopause, which was located near 17.2 km. During the first half of the RI period, this
20 inversion layer weakened throughout Patricia's inner core, with the weakening most pronounced
21 over the developing eye. By the time the storm reached its maximum intensity, the inversion layer
22 over the eye had disappeared almost completely, which was accompanied by an increase in the
23 tropopause height to a level at or above the highest-available dropsonde data point (18.3 km) at
24 two locations. Meanwhile over the eyewall region, the static stability re-strengthened and the
25 tropopause was limited to a level at or below 17.5 km. The mechanisms that led to these changes
26 in upper-level static stability and tropopause height are the subject of the current paper.

27 More recently, Dunion et al. (2014) documented a periodic oscillation of infrared brightness
28 temperature in hurricanes, which they call the "TC diurnal pulse." There will be a whole bunch of
29 papers cited here...

30 At some point (probably in the Discussion) mention the possible importance of static stability
31 asymmetries, in the context of the Dunion diurnal pulse

2. Model Setup

The numerical simulations were performed using version 19.4 of Cloud Model 1 (CM1) described in Bryan and Rotunno (2009) and available online at <http://www2.mmm.ucar.edu/people/bryan/cm1/>. The equations of motion were integrated on a 3000-km-wide, 30-km-deep grid axisymmetric grid with 1-km horizontal and 250-m vertical grid spacing. The computations were performed on an f -plane at 15°N latitude, over a sea surface with constant temperature of 30.5°C, which matches that observed near Hurricane Patricia (2015; Kimberlain et al. 2016). Horizontal turbulence was parameterized using the Smagorinsky scheme described in Bryan and Rotunno (2009, pg. 1773), with a prescribed mixing length that varied linearly from 100 m at a surface pressure of 1015 hPa to 1000 m at a surface pressure of 900 hPa. This formulation allows for realistically-large horizontal mixing lengths near the hurricane’s inner core, consistent with the results of Bryan (2012), while not over-representing horizontal turbulence in convection at outer radii. Vertical turbulence was parameterized using the formulation of Markowski and Bryan (2016, their Eq. 6), using an asymptotic vertical mixing length of 100 m. A Rayleigh damping layer was applied outside of the 2900-km radius and above the 25-km level to prevent spurious gravity wave reflection at the model boundaries. Microphysical processes were parameterized using the Thompson et al. (2004) microphysics scheme and radiative heating tendencies were computed every two minutes using the Rapid Radiative Transfer Model WHAT DOES THE G STAND FOR? (RRTMG) longwave and shortwave schemes (Iacono et al. 2008). A horizontally-homogeneous temperature and humidity field was initialized with a mean sounding computed using all dropsondes deployed during the TCI flight conducted within and around Tropical Storm Patricia on 21 October, 2015 (see Doyle et al. 2017 for details.) Above 19 km, where few TCI observations were available, the temperature profile was taken from the Climate

55 Forecast System Reanalysis (CFSR) grid point nearest Patricia's storm center, valid at 18 UTC
 56 21 October, 2015. Since relative humidity measurements were unreliable at temperatures below
 57 -40°C (Bell et al. 2016), relative humidity was set equal to 50% above 11.5 km (the level above
 58 which temperature dropped below -40°C). The vortex described in Rotunno and Emanuel (1987,
 59 their Eq. 37) was used to initialize the wind field, setting all parameters equal to the values used
 60 therein.

61 3. Budget Computation

62 The static stability can be expressed as the squared Brunt Väisälä frequency:

$$N_m^2 = \frac{g}{T} \left(\frac{\partial T}{\partial z} + \Gamma_m \right) \left(1 + \frac{T}{R_d/R_v + q_s} \frac{\partial q_s}{\partial T} \right) - \frac{g}{1 + q_t} \frac{\partial q_t}{\partial z}, \quad (1)$$

63 where g is gravitational acceleration, T is temperature, R_d and R_v are the gas constants of dry
 64 air and water vapor, respectively, q_s is the saturation mixing ratio, and q_t is the total condensate
 65 mixing ratio. Γ_m is the moist-adiabatic lapse rate:

$$\Gamma_m = \text{DETERMINEWHATTHISISFORTHENON-CONSERVATIVEEQUATIONSET} \quad (2)$$

66 In the tropopause layer, q_s , $\frac{\partial q_s}{\partial T}$, and $\frac{\partial q_t}{\partial z}$ approach zero. In this limiting case, Eq. 1 reduces to:

$$N^2 = \frac{g}{\theta_v} \frac{\partial \theta_v}{\partial z}, \quad (3)$$

67 where g is gravitational acceleration and θ_v is the virtual potential temperature. To compute N^2 ,
 68 CM1 uses Eq. 1 in saturated environments and Eq. 3 in unsaturated environments; for mathemat-
 69 ical simplicity, however, only Eq. 3 will be used for the budget computations herein¹.

70 Taking the time derivative of Eq. 3 yields the static stability tendency:

71 The potential temperature tendency can be partitioned into "budget variables," which are output
 72 directly by the model every two minutes:

¹The validity of this approximation will be substantiated later in this section.

4. Results

Put description of Fig. 1 in this section.

Don't forget to mention 1-2-1 smoother.

a. Static stability evolution

The average N^2 over the first day of the simulation (Fig. 2a) indicates the presence of a static stability maximum about 400 m above the cold-point tropopause. This lower-stratospheric stable layer had begun to erode during the initial spin-up period, with the maximum destabilization occurring at the innermost radii. This decrease in static stability continued into the second day of the simulation (Fig. 2b) as the storm intensified to hurricane strength (Fig. 1). Destabilization was particularly pronounced over the developing eye, where the time-mean cold-point tropopause height increased by up to 400 m compared to the previous day. Over the developing eyewall and outer rainband regions, meanwhile, the tropopause height remained nearly constant. During the third day of the simulation (Fig. 2c), static stability over the eye continued to decrease, and the cold-point tropopause height rose to 18.3 km at the storm center. The tropopause sloped sharply downward over the innermost radii, reaching the 16.4-km level near the 50-km radius. This local minimum in tropopause height corresponded to the eyewall region, where upper-tropospheric static stability increased during this time period. Outside of the eyewall region, static stability began to increase in the layer immediately overlying the cold-point tropopause. This stable layer sloped upward with radius, which corresponded to an upward-sloping tropopause radially outside of the eyewall region. Over the next 24 hours (Fig. 2d), as the storm's maximum 10-m wind speed leveled off near 80 m s^{-1} (Fig. 1), the upper-tropospheric static stability within the eyewall

95 region continued to strengthen, as did the static stability just above the cold-point tropopause
 96 radially outside of the eyewall. As the stable layer strengthened, its altitude rose slightly, which
 97 corresponded to a slight increase in tropopause height outside of the eyewall during this period.
 98 Within the upper troposphere radially outside of the eyewall, meanwhile, static stability decreased
 99 such that it was nearly neutral in a thin layer between the 120- and 150-km radii. The eye region
 100 likewise continued to destabilize, and the cold-point tropopause height increased to a level above
 101 18.5 km. This static stability evolution closely follows that observed in Hurricane Patricia (2015;
 102 Duran and Molinari 2018).

103 *b. Static stability budget analysis*

104 The left column of Fig. 3 depicts 24-hour changes in N^2 over each of the four days of the
 105 simulation. These represent bulk changes computed by subtracting the instantaneous N^2 at the
 106 initial time from the instantaneous N^2 at the final time. The middle column of Fig. 3 represents
 107 the change in N^2 computed using Eq. XXX and the method described in Section 3. The residual
 108 between these two computations (Fig. 3, right column) is much smaller than the change in N^2 ,
 109 meaning that the budget performs well within the analysis domain.

110 To determine which of the budget terms are most important, a time series of the contribution of
 111 each of the budget terms in Eq. XXX to the tropopause-layer static stability tendency is plotted
 112 in Fig. 4. For this figure, each of the budget terms is computed using the method described in
 113 Section 3, except with 1-hour averaging intervals instead of 24-hour intervals. The absolute values
 114 of these tendencies are then averaged over the radius-height domain depicted in Fig. 3 and plotted
 115 as a time series². Advection (Fig. 4, red line) plays an important role in the mean tropopause-

²It will be seen in subsequent figures that each of the terms contributes both positively and negatively to the N^2 tendency within the analysis domain. Thus, taking an average over the domain tends to wash out the positive and negative contributions. To circumvent this problem, the absolute value of each of the terms is averaged, yielding a time series of the mean magnitude of each budget term.

116 layer static stability tendency at all times, and vertical turbulence (Fig. 4, blue line) and radiation
117 (Fig. 4, dark green line) both become important after 48 hours. Although the contribution from
118 horizontal turbulence (Fig. 4, purple line) becomes more important after 72 hours, it is confined
119 to a very small region immediately surrounding the eyewall tangential velocity maximum (not
120 shown), and is negligible throughout the rest of the tropopause layer. The remaining two processes
121 - microphysics and dissipative heating (Fig. 4, orange and light green lines, respectively) - lie atop
122 one another near zero. These time series indicate that, at all times, three budget terms dominate the
123 tropopause-layer static stability tendency: advection, vertical turbulence, and radiation. Variations
124 in the magnitude and spatial structure of these terms drive the static stability changes depicted in
125 Fig. 2; subsequent sections will focus on these variations and what causes them.

126 *(i) 0-24 hours* The first 24 hours of the simulation was characterized by a weakening of the
127 lower-stratospheric static stability maximum above 17 km (Fig. ??a, purple shading) and an in-
128 crease in static stability below (green shading). Although these tendencies extended out to the
129 200-km radius, they were particularly pronounced at innermost radii. A comparison of the contri-
130 butions of advection (Fig. ??b), vertical turbulence (Fig. ??c), and radiation (Fig. ??d) reveals that
131 advection is primarily responsible for the change in static stability during this period. ...Explain
132 this in the context of radial and vertical velocities...

133 *(ii) 24-48 hours* During the second day of the simulation, the lower-stratospheric stable layer
134 continued to weaken (Fig. 6a). This weakening trend in the 16.75-17.75-km layer extended from
135 the 50 km radius outward to past 200 km, and was primarily driven by advection (Fig. 6b). Below
136 this layer, static stability began to increase slightly. This stabilization had contributions from both
137 vertical turbulence (Fig. 6c) and radiation (Fig. 6d) in the 16-16.5-km layer. ...Explain this in
138 context of mean vertical mixing coefficient and mean radiative heating tendency... Meanwhile,

139 radially inward of 60 km, static stability below 17.5 km continued to weaken, primarily due to
140 advective processes.

141 *(iii) 48-72 hours* The third day of the simulation marked a dramatic change in the structure of the
142 tropopause-layer static stability tendencies. During this time, static stability increased markedly
143 in an upward-sloping region within the 30-60-km radial band (Fig. 7a), and also increased within
144 the 16.75-17.5-km layer out to at least the 200-km radius. As this layer stabilized, the layer
145 immediately below it destabilized in a broad region extending from 60-200 km. Examination
146 of the contribution from total advection (Fig. 7b) reveals that advection no longer dominates the
147 static stability tendencies. Instead, a combination of vertical turbulence (Fig. 7c) and radiation
148 (Fig. 7d) overcomes the destabilizing influence of advection to create the layer of increasing static
149 stability. Meanwhile, the destabilizing influence of vertical turbulence in a broad region below
150 17 km combines with a small region of destabilization due to radiation in the 50-120-km radial
151 band combine to destabilize the layer below 16.5 km in the 50-200-km radial band. Comparing
152 the sum of advection and vertical turbulence (Fig. 7e) to the sum of advection, vertical turbulence,
153 and radiation (Fig. 7f) reveals that radiation plays a fundamental role in the re-strengthening of the
154 lower-stratospheric stable layer during this time.

155 *(iv) 72-96 hours*

156 **5. Discussion**

157 Dunion et al. speculate that the diurna pulse only occurs in mature storms. Maybe the develop-
158 ment of the near-tropopause stable layer could partially explain the reason for this.

159 *Acknowledgments.* We are indebted to Dr. George Bryan for his continued development and
160 support of Cloud Model 1. We also thank Drs. Jeffrey Kepert, Robert Fovell, and Erika Navarro
161 for fruitful conversations related to this work. ADD GRANT NUMBER

162 **References**

163 Bell, M. M., and Coauthors, 2016: Office of Naval Research Tropical Cyclone Intensity (TCI)
164 2015 NASA WB-57 High Density Dropsonde Sounding System (HDSS) data, version 1.0. doi:
165 10.5065/D6KW5D8M.

166 Bryan, G. H., 2012: Effects of surface exchange coefficients and turbulence length scales on the
167 intensity and structure of numerically simulated hurricanes. *Mon. Wea. Rev.*, **140**, 1125–1143.

168 Bryan, G. H., and R. Rotunno, 2009: The maximum intensity of tropical cyclones in axisymmetric
169 numerical model simulations. *Mon. Wea. Rev.*, **137**, 1770–1789.

170 Doyle, J. D., and Coauthors, 2017: A view of tropical cyclones from above: The Tropical Cyclone
171 Intensity (TCI) Experiment. *Bull. Amer. Meteor. Soc.*, **98**, 2113–2134.

172 Dunion, J. P., C. D. Thorncroft, and C. S. Velden, 2014: The tropical cyclone diurnal cycle of
173 mature hurricanes. *Mon. Wea. Rev.*, **142**, 3900–3919.

174 Duran, P., and J. Molinari, 2018: Dramatic inner-core tropopause variability during the rapid
175 intensification of Hurricane Patricia (2015). *Mon. Wea. Rev.*, **XXX**, XXX–XXX.

176 Iacono, M. J., J. S. Delamere, E. J. Mlawer, M. W. Shephard, S. A. Clough, and W. D. Collins,
177 2008: Radiative forcing by long-lived greenhouse gases: Calculations with the AER radiative
178 transfer models. *J. Geophys. Res.*, **113** (D13103).

179 Kimberlain, T. B., E. S. Blake, and J. P. Cangialosi, 2016: Tropical cyclone report: Hurricane
180 Patricia. National Hurricane Center. [Available online at www.nhc.noaa.gov].

181 Markowski, P. M., and G. H. Bryan, 2016: LES of laminar flow in the PBL: A potential problem
182 for convective storm simulations. *Mon. Wea. Rev.*, **144**, 1841–1850.

183 Rogers, R. F., S. Aberson, M. M. Bell, D. J. Cecil, J. D. Doyle, J. Morgerman, L. K. Shay, and
184 C. Velden, 2017: Re-writing the tropical record books: The extraordinary intensification of
185 Hurricane Patricia (2015). *Bull. Amer. Meteor. Soc.*, **98**, 2091–2112.

186 Rotunno, R., and K. A. Emanuel, 1987: An air-sea interaction theory for tropical cyclones. Part II:
187 Evolutionary study using a nonhydrostatic axisymmetric numerical model. *J. Atmos. Sci.*, **44**,
188 542–561.

189 Thompson, G., R. M. Rasmussen, and K. Manning, 2004: Explicit forecasts of winter precipitation
190 using an improved bulk microphysics scheme. Part I: Description and sensitivity analysis. *Mon.*
191 *Wea. Rev.*, **132**, 519–542.

LIST OF FIGURES

192			
193	Fig. 1.	The maximum 10-m wind speed (top panel; m s^{-2}) and minimum sea-level pressure (bottom	
194		panel; hPa) in the simulated storm (blue lines) and from Hurricane Patricia's best track (red	
195		stars).	13
196	Fig. 2.	Twenty-four-hour averages of squared Brunt-Väisälä frequency (10^{-4} s^{-2}) over the first four	
197		days of the simulation. Orange lines represent the cold-point tropopause computed from the	
198		mean temperature field over the same time periods.	14
199	Fig. 3.	Left panels: Twenty-four-hour changes in squared Brunt-Väisälä frequency (10^{-4} s^{-2}) over	
200		(a) 0-24 hours, (b) 24-48 hours, (c) 48-72 hours, (d) 72-96 hours. Middle Panels: The N^2	
201		change over the same time periods computed using Eq. XXX. Right Panels: The budget	
202		residual over the same time periods, computed by subtracting the budget change (middle	
203		column) from the model change (left column).	15
204	Fig. 4.	Time series of the contribution of each of the budget terms to the time tendency of the	
205		squared Brunt-Väisälä frequency (N^2 ; 10^{-4} s^{-2}). For each budget term, the absolute value	
206		of the N^2 tendency is averaged both temporally over 1-hour periods (using output every	
207		minute), and spatially within the radius-height domain depicted in Fig. 3.	16
208	Fig. 5.	(a) Total change in N^2 over the 0-24-hour period ($10^{-4} \text{ s}^{-2} (24 \text{ hr})^{-1}$) and the contributions	
209		to that change from (b) the sum of horizontal and vertical advection, (c) vertical turbulence,	
210		and (d) the sum of longwave and shortwave radiation.	17
211	Fig. 6.	As in Fig. 5, but for the 24-48-hour period.	18
212	Fig. 7.	(a) Total change in N^2 over the 48-72-hour period ($10^{-4} \text{ s}^{-2} (24 \text{ hr})^{-1}$) and the contributions	
213		to that change from (b) the sum of horizontal and vertical advection, (c) vertical turbulence,	
214		(d) the sum of longwave and shortwave radiation, (e) the sum of horizontal advection, ver-	
215		tical advection, and vertical turbulence, and (f) the sum of horizontal advection, vertical	
216		advection, vertical turbulence, and longwave and shortwave radiation.	19
217	Fig. 8.	As in Fig. 7, but for the 72-96-hour period.	20
218	Fig. 9.	Radial velocity (m s^{-1} ; filled contours), potential temperature (K; thick black contours), and	
219		cold point tropopause height (orange line) averaged over (a) 0-24 hours, (b) 24-48 hours, (c)	
220		48-72 hours, and (d) 72-96 hours.	21
221	Fig. 10.	Vertical velocity (cm s^{-1} ; filled contours), potential temperature (K; thick black contours),	
222		and cold point tropopause height (orange line) averaged over (a) 0-24 hours, (b) 24-48 hours,	
223		(c) 48-72 hours, and (d) 72-96 hours.	22
224	Fig. 11.	Total condensate mixing ratio (g kg^{-1}) and cold point tropopause height (orange line) aver-	
225		aged over (a) 0-24 hours, (b) 24-48 hours, (c) 48-72 hours, and (d) 72-96 hours.	23

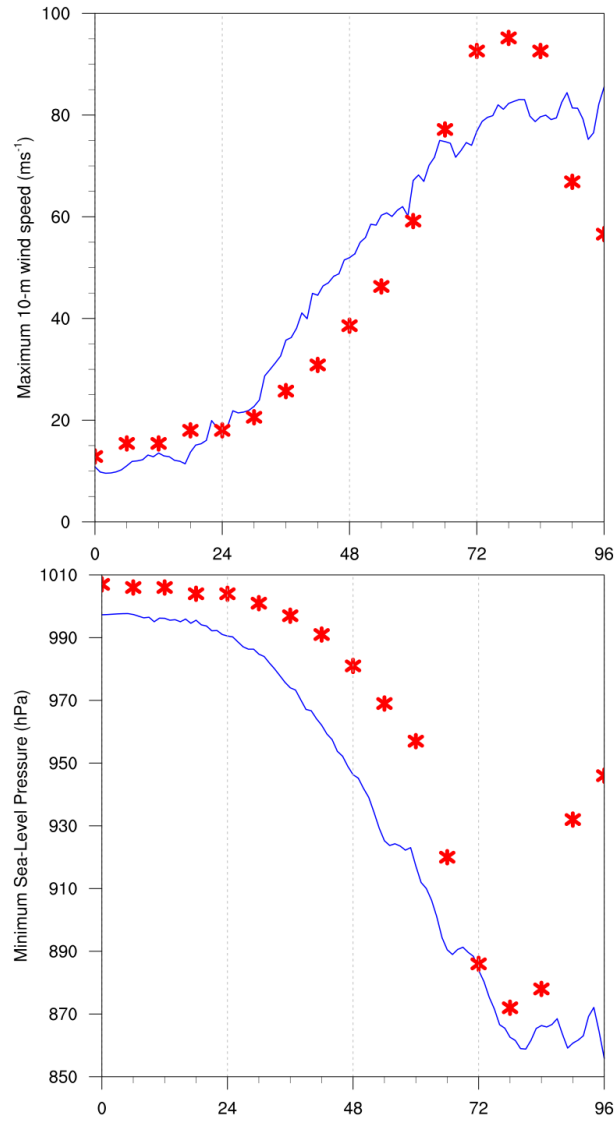


FIG. 1. The maximum 10-m wind speed (top panel; m s^{-2}) and minimum sea-level pressure (bottom panel; hPa) in the simulated storm (blue lines) and from Hurricane Patricia's best track (red stars).

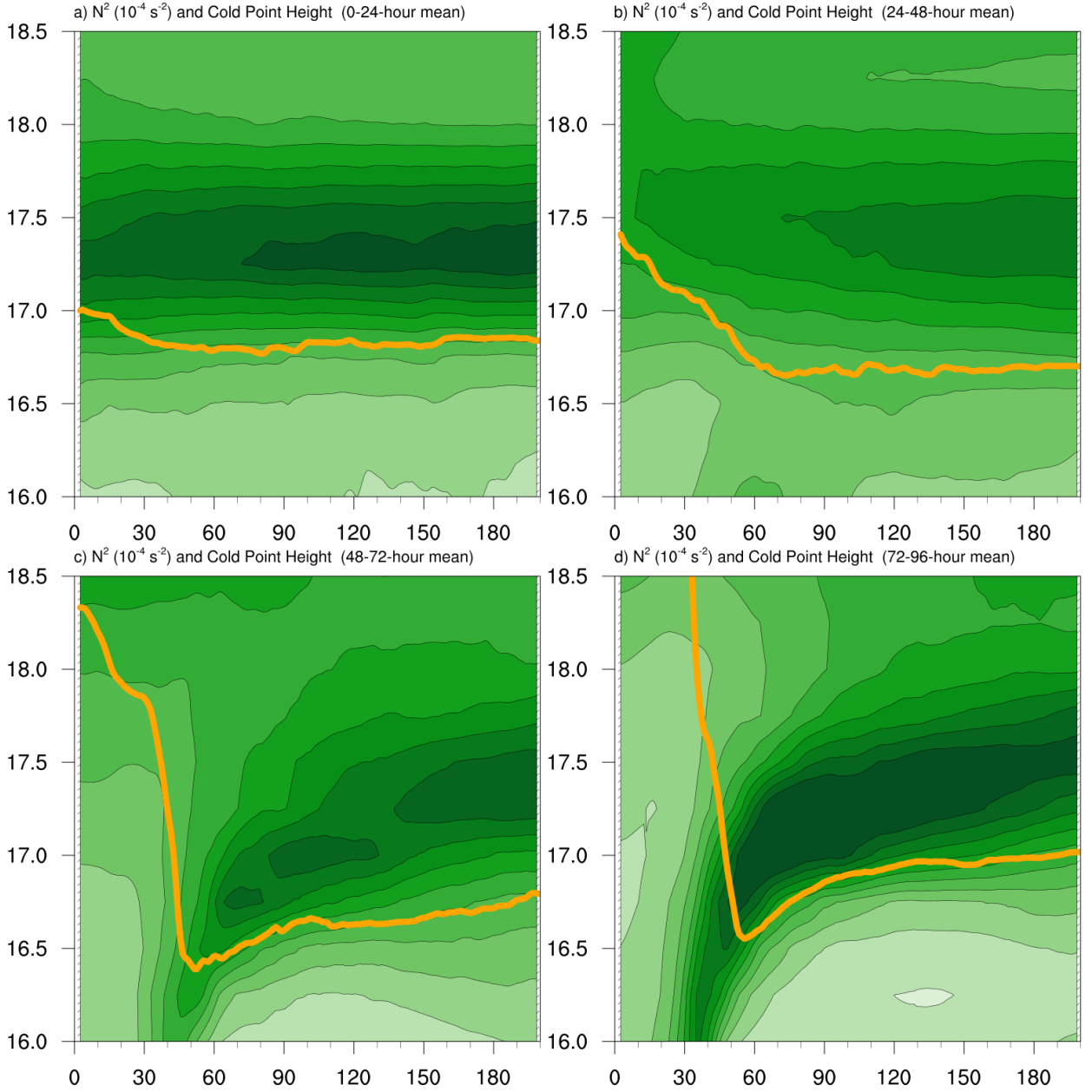


FIG. 2. Twenty-four-hour averages of squared Brunt-Väisälä frequency (10^{-4} s^{-2}) over the first four days of the simulation. Orange lines represent the cold-point tropopause computed from the mean temperature field over the same time periods.

figures/fig03_R-Z_mod+bud+res.png

231 FIG. 3. Left panels: Twenty-four-hour changes in squared Brunt-Väisälä frequency (10^{-4} s^{-2}) over (a) 0-24
232 hours, (b) 24-48 hours, (c) 48-72 hours, (d) 72-96 hours. Middle Panels: The N^2 change over the same time
233 periods computed using Eq. XXX. Right Panels: The budget residual over the same time periods, computed by
234 subtracting the budget change (middle column) from the model change (left column).



figures/fig04_AVG_budterms.png

235 FIG. 4. Time series of the contribution of each of the budget terms to the time tendency of the squared
236 Brunt-Väisälä frequency (N^2 ; 10^{-4} s^{-2}). For each budget term, the absolute value of the N^2 tendency is averaged
237 both temporally over 1-hour periods (using output every minute), and spatially within the radius-height domain
238 depicted in Fig. 3.

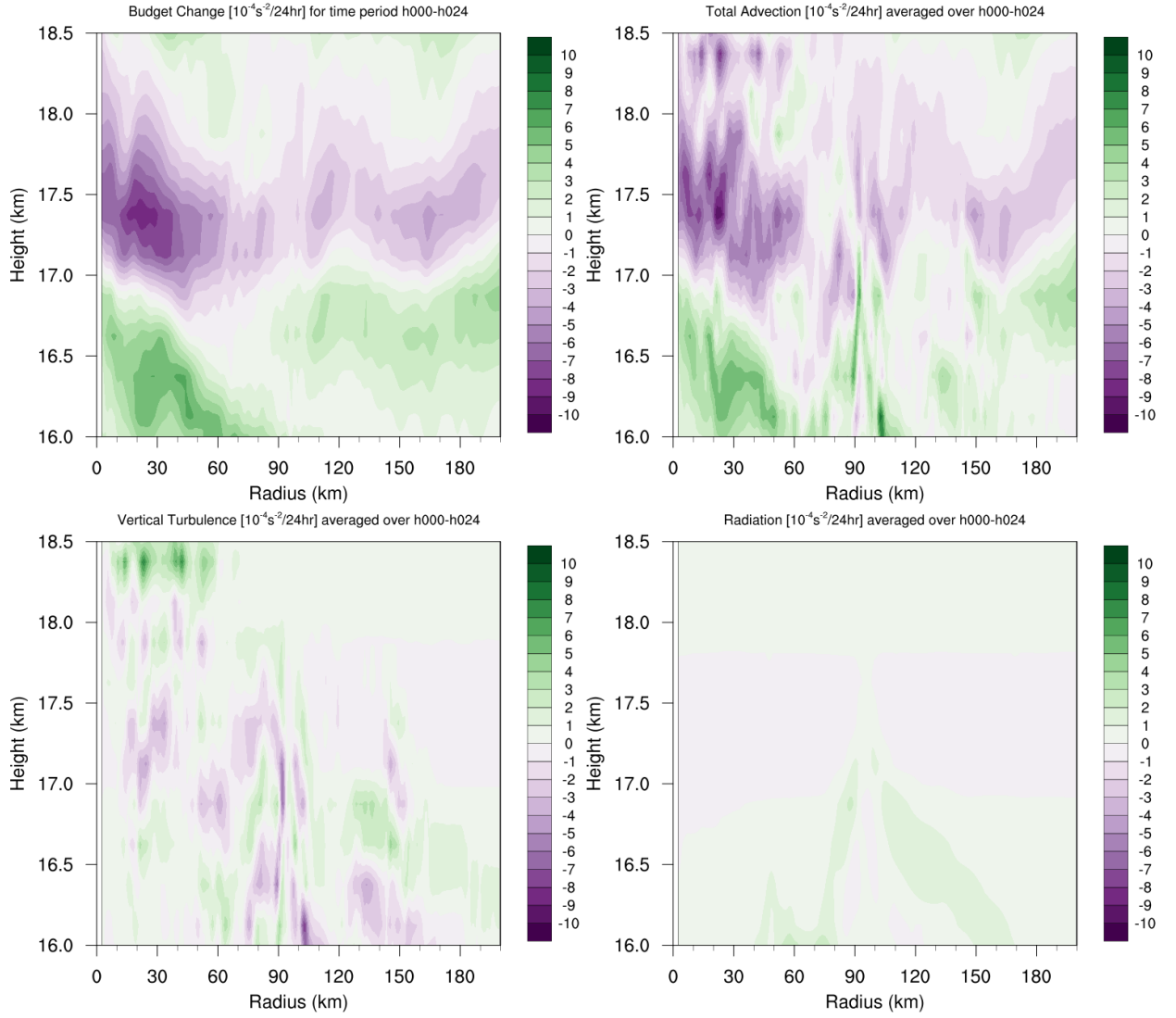


FIG. 5. (a) Total change in N^2 over the 0-24-hour period ($10^{-4} \text{ s}^{-2} (24 \text{ hr})^{-1}$) and the contributions to that change from (b) the sum of horizontal and vertical advection, (c) vertical turbulence, and (d) the sum of longwave and shortwave radiation.

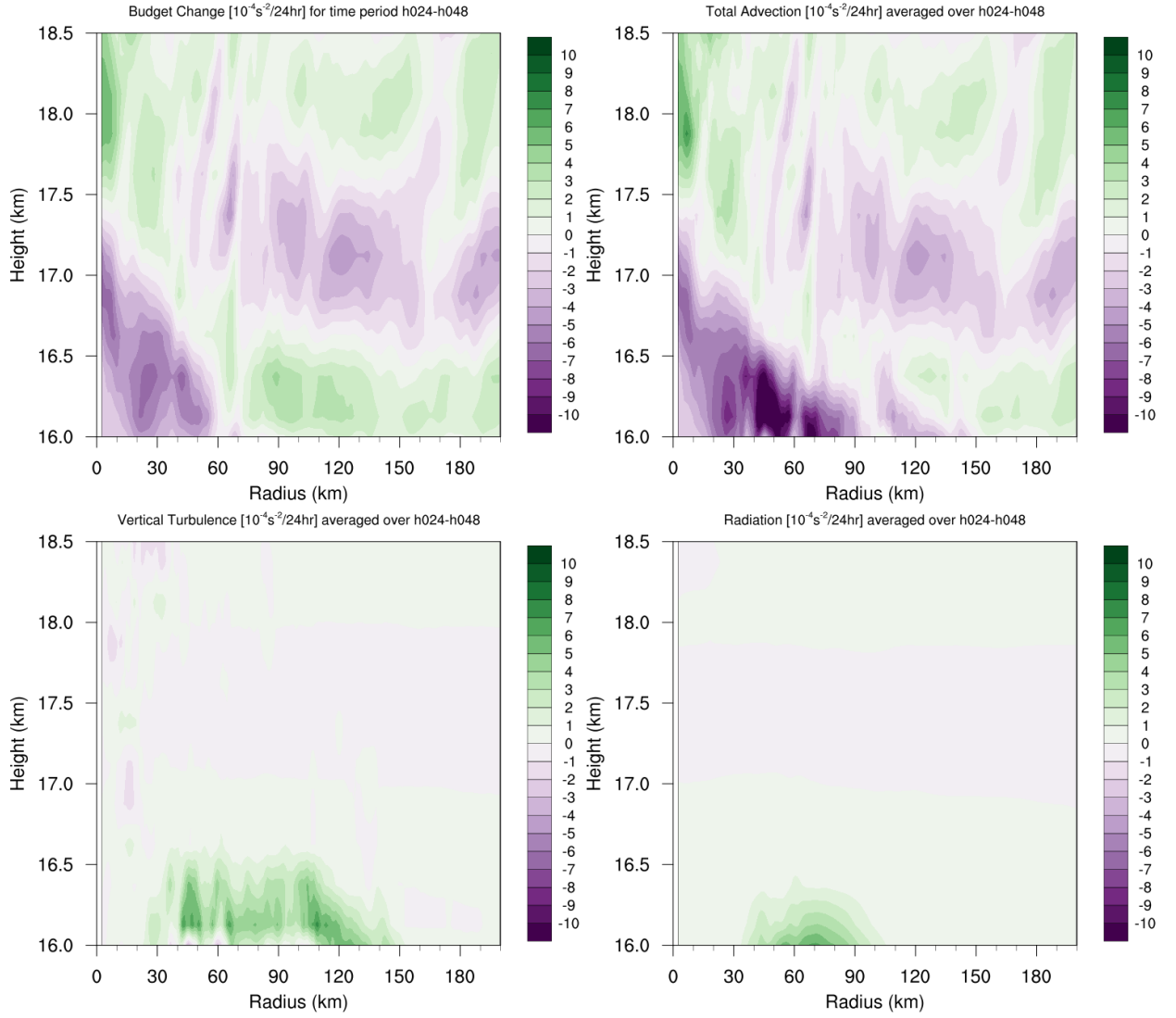



FIG. 6. As in Fig. 5, but for the 24-48-hour period.



figures/fig07_h048-h072-budgetterms.png

242 FIG. 7. (a) Total change in N^2 over the 48-72-hour period ($10^{-4} \text{ s}^{-2} (24 \text{ hr})^{-1}$) and the contributions to that
243 change from (b) the sum of horizontal and vertical advection, (c) vertical turbulence, (d) the sum of longwave
244 and shortwave radiation, (e) the sum of horizontal advection, vertical advection, and vertical turbulence, and (f)
245 the sum of horizontal advection, vertical advection, vertical turbulence, and longwave and shortwave radiation.

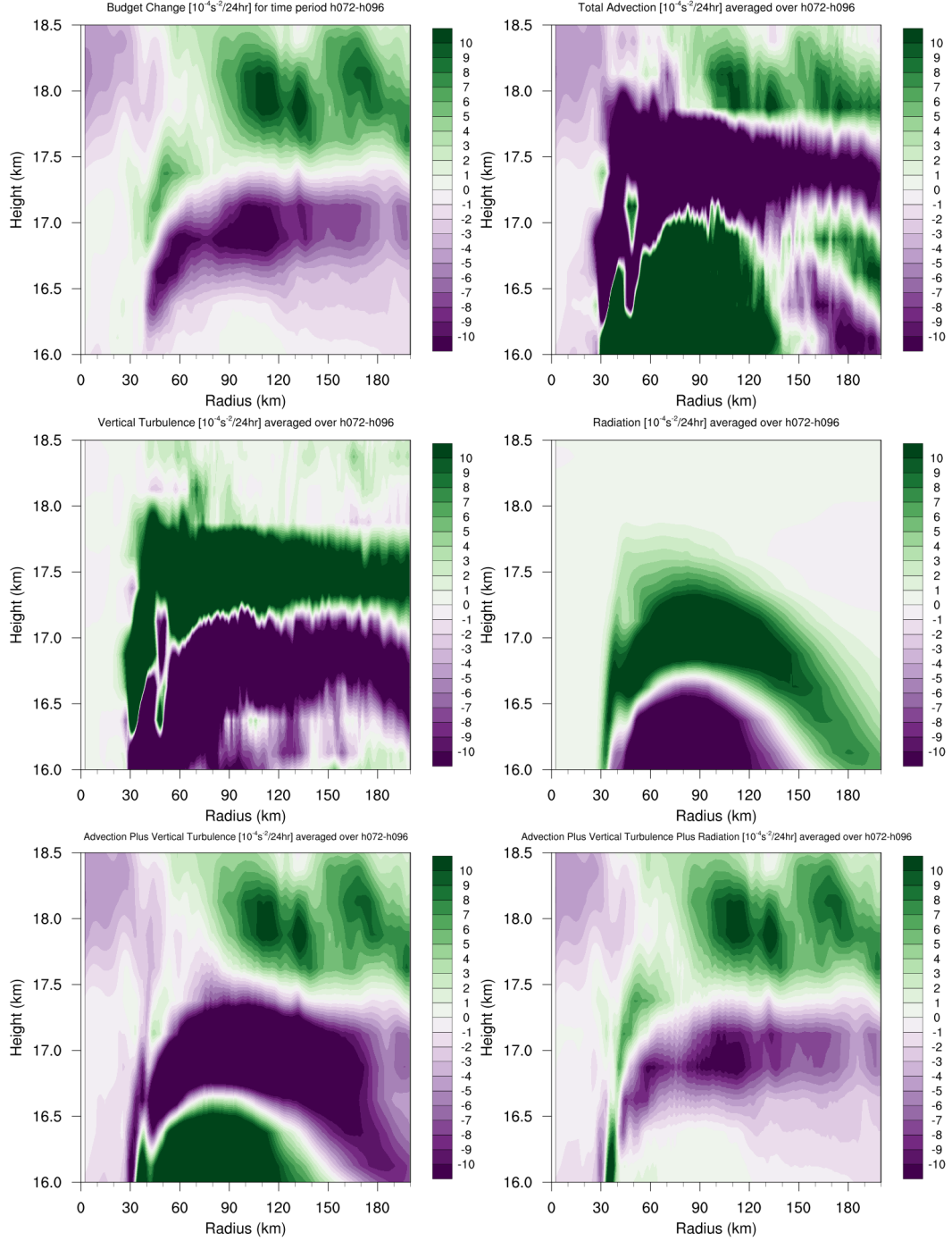


FIG. 8. As in Fig. 7, but for the 72-96-hour period.

figures/fig09_u.png

246 FIG. 9. Radial velocity (m s^{-1} ; filled contours), potential temperature (K; thick black contours), and cold point
247 tropopause height (orange line) averaged over (a) 0-24 hours, (b) 24-48 hours, (c) 48-72 hours, and (d) 72-96
248 hours.

figures/fig10_w.png

249 FIG. 10. Vertical velocity (cm s^{-1} ; filled contours), potential temperature (K; thick black contours), and cold
250 point tropopause height (orange line) averaged over (a) 0-24 hours, (b) 24-48 hours, (c) 48-72 hours, and (d)
251 72-96 hours.

figures/fig11_qtot.png

252 FIG. 11. Total condensate mixing ratio (g kg^{-1}) and cold point tropopause height (orange line) averaged over
253 (a) 0-24 hours, (b) 24-48 hours, (c) 48-72 hours, and (d) 72-96 hours.